

Automated Detection of Mitosis in Embryonic Tissues

Parthipan Siva
University of Waterloo
VIP Lab
Waterloo, Canada
psiva@uwaterloo.ca

G. Wayne Brodland
University of Waterloo
Embryo Biomechanics Group
Waterloo, Canada
brodland@uwaterloo.ca

David Clausi
University of Waterloo
VIP Lab
Waterloo, Canada
dclausi@uwaterloo.ca

Abstract

Characterization of mitosis is important for understanding the mechanisms of development in early stage embryos. In studies of cancer, another situation in which mitosis is of interest, the tissue is stained with contrast agents before mitosis characterization; an intervention that could lead to atypical development in live embryos. A new image processing algorithm that does not rely on the use of contrast agents was developed to detect mitosis in embryonic tissue. Unlike previous approaches that uses still images, the algorithm presented here uses temporal information from time-lapse images to track the deformation of the embryonic tissue and then uses changes in intensity at tracked regions to identify the locations of mitosis. On a one hundred minute image sequence, consisting of twenty images, the algorithm successfully detected eighty-one out of the ninety-five mitosis. The performance of the algorithm is calculated using the geometric mean measure as 82%. Since no other method to count mitoses in live tissues is known, comparisons with the present results could not be made.

1. Introduction

Studies of embryo development [1] have shown that mitosis (*cell division*) rate and orientation can play a significant role in tissue growth and elongation. To correlate local tissue deformations in embryos with mitosis frequency and direction, an algorithm to quantify mitosis in time-lapse images of the embryo was required. This requirement is part of a larger research program to quantify birth defects in developing embryos [2].

Two approaches have been considered for identifying mitosis. The first approach involves counting the number of cells in each frame by isolating and tracking all the cells in the image sequence. This approach will yield the frequency and orientation of mitosis as well as the lineage of individual cells. The second approach involves locating where

mitosis is occurring in each frame based on local features. Unlike the first approach, this approach will only yield the frequency and orientation of the mitosis, because individual cells are not tracked.

For the first approach, based on cell counting, all cells in the embryonic tissue must be segmented. Existing segmentation techniques [13, 15] rely on high contrast images, where cell boundaries are clearly visible and thus can not be used reliably for embryonic tissue images [6] (Figure 1). There are also methods for counting cells in cell cultures [11]. These methods are meant for situations where individual cells are isolated from each other, not for cases where cells are closely packed as they are in embryonic tissues.

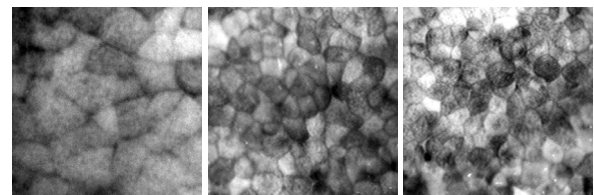


Figure 1. Images of Embryonic Tissue.

The second approach, using local features, has been successfully used to detect mitosis in still images of stained cancer tissues [7, 8], by locating the resulting compact, dark regions with highly uneven boundaries. The embryonic tissue images (Figure 1) are somewhat similar to the cancer tissue images (Figure 2), but mitotic cells in embryonic tissues are not necessarily the darkest regions in the image (Figure 3). In the case of cancer tissue, mitotic cells are made to be the darkest region by carefully controlling the staining and imaging conditions of the tissue. When imaging embryo development, stains can not be used since stains will influence live embryo development. As a result, specialized image processing methods must be employed.

Similar to [7] and [8], a method for identifying mitosis based on gray scale intensity analysis is presented here.

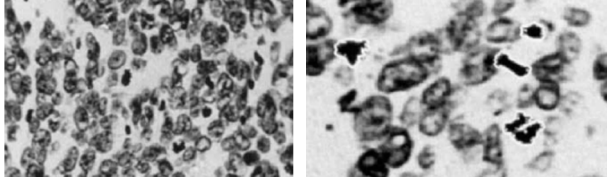


Figure 2. Images of Cancer Tissue [8]. Mitosis is outlined in white on the right image.

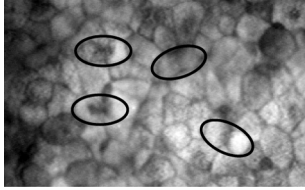


Figure 3. Image of Embryonic Tissue with Mitosis. The mitosis regions, circled, are not the darkest regions in the image.

Unlike [7] and [8], this approach uses temporal information to detect regions which decrease in gray scale intensity, instead of finding dark regions in a single still image. The intensity decrease is caused by the nucleus division as seen in Figure 4. In order to detect these intensity changes, direct frame differencing can not be applied due to tissue displacement and deformation between frames. Each pixel might be tracked from one frame to the next before comparing pixel intensity. However, this process is too computationally expensive and not all pixels can be uniquely tracked from one frame to the next. Instead, the algorithm presented here tracks local regions using a triangular mesh. Frame differencing between corresponding regions is then used to identify mitosis.

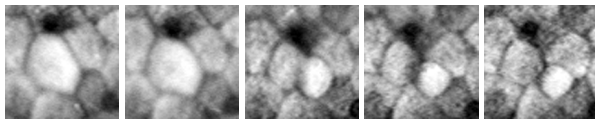


Figure 4. Single Mitosis.

2. Deformable Grid Tracking

Before mitosis can be identified by studying intensity drops in embryonic tissue, corresponding tissue segments between frames must be identified. This can be accomplished by deforming a triangular mesh between frames [10], such that the corresponding triangles on the frames correspond to the same region of tissue.

The triangular mesh at frame T can be represented by a set of vertices $S_T = \{\vec{v}_1, \dots, \vec{v}_L\}^T$, where \vec{v} is the image coordinate of a single vertex. Then tracking the triangular mesh from frame T to frame $T + 1$ becomes a question of tracking the set of vertices S_T to frame $T + 1$. Each of the vertices can be tracked from frame T to $T + 1$ using local features [14], however, some vertices might not have sufficiently accurate local features to be tracked. An alternate method is preferred.

An alternative to tracking each vertex is to first track a set of key points F_T , that have unique local features, from frame T to $T + 1$. Then using the original location of the key points F_T , and the tracked location of the key points \hat{F}_{T+1} , the triangular mesh from frame T (S_T) can be tracked to frame $T + 1$ (S_{T+1}) [10].

2.1 Key Point Selection

The set of key points F_T to be tracked to frame $T + 1$, can be chosen by analyzing the current frame for locations that are suitable for tracking and ignoring any previous points that were tracked from frame $T - 1$ to frame T . However, ignoring the previously tracked points is not advisable because statistical trackers such as the Kalman Filters [5] need to track a point over multiple frames before converging. Therefore, the set of key points for tracking F_T are selected from the set of tracked points \hat{F}_T and the set of points suitable for tracking (A_T) in the current frame.

A tracked point is kept as a key point while it is still a suitable point for tracking. The probability of a tracked point, $\hat{F}_T(i)$ being a suitable point for tracking in frame T can be determined given all points in frame T that are suitable for tracking A_T .

$$P(i) = \exp \left(\frac{\left[\min \left(\left\| \hat{F}_T - \vec{a} \right\| \right) \right]^2}{-2\sigma^2} \right), \quad (1)$$

$\forall \vec{a} \in A_T.$

Anchor points $A_T = \{\vec{a}_1, \dots, \vec{a}_L\}^T$ are the set of all points in frame T that are suitable for tracking, where \vec{a} is the image coordinate of a single point. The value of σ allows for some variability in the closeness of the tracked point to an anchor point in the current frame.

A point from \hat{F}_T is added to F_T if the average of its probability of being an anchor point using (1) for the last X frames is above P_{Thresh} . An average is used because an anchor point tracked over multiple frames can have one or two frames where the probability is low due to focus or illumination problems. The parameters X and P_{Thresh} were chosen empirically based on studying a time-lapse images of embryos from a training image sequence: $X = 4$ and $P_{Thresh} = 0.5$.

Once all relevant points from \hat{F}_T are added to F_T , the remaining space in F_T is filled with points from A_T such that points added from A_T are within Δ_{MAX} from the closest point in F_T . Δ_{MAX} is the maximum possible displacement of an anchor point between frame T and $T + 1$. In the first frame where tracked points, $\hat{F}_{T=0}$, are not available, the key points are selected as all anchor points in the frame.

2.2 Anchor Points

In Section 2.1, the anchor points A_T for each time frame T is assumed to be given. For a user to manually select all anchor points in each frame is too tedious. Therefore, in this section a method for automatically selecting anchor points is presented.

Anchor points are all points in the current frame that are suitable for tracking. To isolate the points that are suitable for tracking, all points on the cell sheet are classified as either lying inside a cell, on a boundary between two cells or on a junction between multiple cells. When tracking points using local region information, only junction points can be tracked uniquely to the next frame as seen in Figure 5. This problem is called the *aperture problem* and occurs in all local region based tracking schemes [12]. As a result of the aperture problem, only junction points are selected as anchor points.

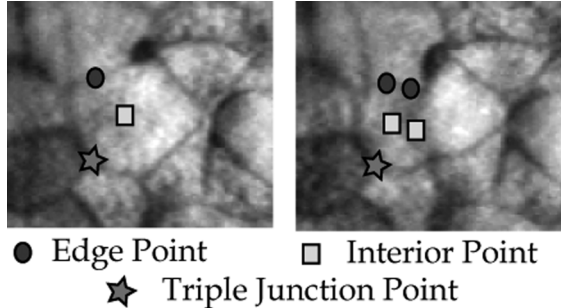


Figure 5. Matching edge, inside and junction points between frames. Only junction points can be uniquely matched.

The junction points can be detected by finding intersections of cell boundaries. To isolate all junction points, all cell boundaries need to be found such that each individual cell is segmented in the image. However, as stated before, due to lack of contrast not all cells can be segmented. Therefore, only junction points between boundaries with high enough contrast will be detected as anchor points.

To detect those boundaries with high contrast the Gabor filter (GF) is used. The use of the GF to detect cell boundaries was successfully demonstrated in electron microscopy images [13]. Four GFs, as formulated in [13], are used to

detect cell boundaries. All four filters are tuned to a line width of 5 pixels and a line spread of 10 pixels; converting line width and spread to the frequency and bandwidth of the Gabor filter is presented in [13]. The four filters have an orientations of $-45^\circ, 0^\circ, 45^\circ$ and 90° .

The magnitude of the real part of the Gabor filtered images can be combined to determine the magnitude of the cell boundaries. The four filtered images I_{-45}^{RGF} , I_0^{RGF} , I_{45}^{RGF} and I_{90}^{RGF} are first combined in pairs to get two estimates of the edge magnitude. The first estimate \hat{B}_1 is obtained in (2) using the 0° and 90° orientation filters. These two orientations of the GF will give high responses for horizontal and vertical boundaries but weaker responses for diagonal boundaries. The second estimate \hat{B}_2 is obtained in (3) using the -45° and 45° orientation filters. These two orientations of the GF will give high responses for diagonal boundaries and weaker responses for horizontal and vertical boundaries. The two boundary estimates are then combined in (4) to obtain a more accurate estimation of cell boundary strengths in all orientations.

$$\hat{B}_1 = \sqrt{(I_0^{RGF})^2 + (I_{90}^{RGF})^2} \quad (2)$$

$$\hat{B}_2 = \sqrt{(I_{-45}^{RGF})^2 + (I_{45}^{RGF})^2} \quad (3)$$

$$B = \max(\hat{B}_1, \hat{B}_2) \quad (4)$$

Erroneous boundaries are then eliminated by thresholding $I_{filtered}$ with the phase response of the Gabor filter. All boundary points having a phase response between 170° to 190° are kept as potential cell boundaries. The potential boundaries are then thresholded to a binary image and thinned to one pixel width using a morphological skeletonization operation [3]. The resulting binary boundary image is then used to obtain junction points.

Given the binary boundary image, all junctions between three boundary segments are detected as junction points. Initial guesses of these triple junction points are obtained by filtering the binary boundary image using all four 90° rotations for each of the three masks shown in Figure 6. These initial guesses are then improved by checking the lengths of each of the three branches meeting at the junction point. The reasoning behind this is that not all detected boundaries are actual cell boundaries. These noise boundaries, created by illumination defects, will not be as long as actual cell boundaries.

To check the length of the branches, a circle of radius R ($R \approx 5$ pixels) is placed on each of the potential junction points. The point is kept as a junction point if the three branches from the potential junction point reach the circumference of the circle without touching each other. This can be determined by using the following two rules:

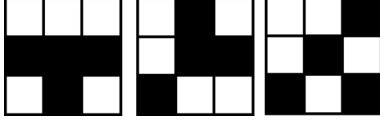


Figure 6. Masks used to find triple junction points.

1. There are any three boundary points on the circumference of the circle that are directly connected to the junction point.
2. If the junction point is removed, the three boundary points on the circumference are no longer connected.

Figure 7 illustrates some valid and invalid junction points based on the above two rules.

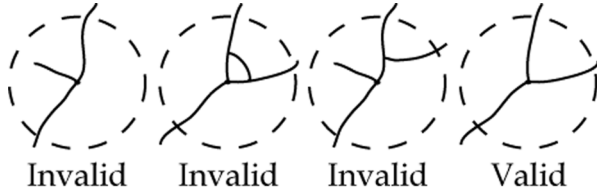


Figure 7. Invalid and valid triple junction points based on the branch length test using a circle.

Of the detected junction points, all points that are Δ_{MAX} distance apart from each other are chosen as anchor points A_T .

2.3 Tracking Key Points

Once the set of key points F_T are selected they need to be tracked from frame T to $T+1$ before the triangular mesh S_T can be deformed from frame T to $T+1$ relative to these key points. Tracking of key points F_T from frame T to $T+1$ is accomplished using a Kalman Filter (KF) [5]. A velocity based model with position measurements as defined in equations (5),(6) and (7) is used.

$$\vec{z} = [x \quad y \quad v_x \quad v_y]^T \quad (5)$$

$$\vec{z}(t+1) = \begin{bmatrix} 1 & 0 & \Delta t & 0 \\ 0 & 1 & 0 & \Delta t \\ 0 & 0 & 1 & 0 \\ 0 & 0 & 0 & 1 \end{bmatrix} \vec{z}(t) + I\vec{\omega}(t) \quad (6)$$

$$\vec{m}(t) = \begin{bmatrix} 1 & 0 & 0 & 0 \\ 0 & 1 & 0 & 0 \end{bmatrix} \vec{z}(t) + \vec{V}(t) \quad (7)$$

Here $\vec{\omega}(t) \sim N(\vec{0}, P)$, $\vec{V}(t) \sim N(\vec{0}, R)$, (x, y) is the location of the point, (v_x, v_y) is the velocity of the point and $\vec{m}(t)$ is the measured location of the point. The initial covariance matrices P and R are chosen as diagonal matrices with large value along the diagonal. This weighting ensures that the measurement is weighed more than the KF prediction at the start.

The displacement measurement of a point in F_T from frame T to $T+1$ needed for the KF is obtained by matching phase responses of the point from frame T to all points in a local N by N neighborhood of the KF's predicted location in frame $T+1$. The matching in the local N by N neighborhood is accomplished using the phase disparity measurement developed in [4]. The phase disparity measure was chosen over the spatial correlation method presented in [14], because phase response was shown to be more robust against illumination and perspective deformations [4].

The covariance matrix for the measurement is obtained as the variance of the phase disparity measures in the local N by N neighborhood [12]. The local neighborhood size N is chosen as $2\Delta_{MAX}$.

The phase response used for tracking is obtained from a Gabor filter bank with twelve filters. Each of the twelve filters were tuned in the same manner as in Section 2.2. The filters were tuned for three line widths of 5, 10 and 15 pixels. For each of the three line widths, a Gabor filter at orientations of $-45^\circ, 0^\circ, 45^\circ$ and 90° were used.

2.4 Grid Fitting

In grid fitting, the triangular mesh from frame T needs to be transformed to frame $T+1$ relative to the tracked key points. That is, the locations of the triangular mesh vertices at frame $T+1$, S_{T+1} , need to be estimated based on S_T , F_T and \hat{F}_{T+1} . The algorithm presented in [10] is applied for this with slight modifications.

The deformed grid S_{T+1} is estimated by minimizing the objective function $\epsilon(S_{T+1})$ [10].

$$\epsilon(S_{T+1}) = \epsilon_D(S_{T+1}) + \epsilon_C(S_T, S_{T+1}, F_T, \hat{F}_T) \quad (8)$$

ϵ_D represents a limit on the mesh deformation and ϵ_C represents the correspondence between the anchor points from frame T and the points tracked to frame $T+1$.

2.4.1 Deformation Constraint

The deformation can be limited using a second order derivative constraint, namely, the tissue is only allowed to deform smoothly like a rubber sheet that is being stretched. A similar constraint was used in the previous work on tracking points on the deformable tissue [14].

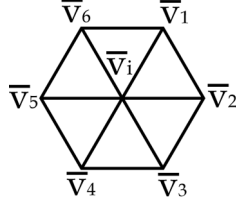


Figure 8. Mesh vertex \vec{v}_i and its 6 neighbors.

Given a point on the triangular mesh and all its neighbors, as illustrated in Figure 8, the smoothness constraint for point i can be written as

$$\epsilon_{D_i} = (2\vec{v}_i - \vec{v}_1 - \vec{v}_4) + (2\vec{v}_i - \vec{v}_2 - \vec{v}_5) + (2\vec{v}_i - \vec{v}_3 - \vec{v}_6) \quad (9)$$

The second derivative constraint (10) for all points on the mesh can be written using a sparse, banded matrix K , so that the constraint follows the formulation in [10].

$$\epsilon_D(S_{T+1}) = 1/2(X^T K X + Y^T K Y). \quad (10)$$

2.4.2 Correspondence Constraint

The correspondence constraint, used for grid fitting, is obtained from [10] as

$$\epsilon_C(S_T, S_{T+1}, F_T, \hat{F}_T) = - \sum_{i=1}^K \rho(\|\hat{F}_T(i) - T_S(F_T(i), S_{T+1}, S_T)\|, r) \quad (11)$$

where $i = 1 \dots M$ and $T_S()$ transforms an anchor point from frame T to frame $T+1$ with respect to the triangular mesh using Barycentric triplets [10].

In [10], ρ , from (11), is given as

$$\rho(\delta, r) = \begin{cases} \frac{3(r^2 - \delta^2)}{4r^3} & \delta < r \\ 0 & \text{otherwise.} \end{cases}$$

The $\delta < r$ check is performed in [10] because in their case the anchor points have one to many mapping. That is, an anchor point in frame T is matched to multiple potential points in frame $T+1$ because in object detection there can be large translations, rotations and perspective changes. In the case of tracking within consecutive frames of an image sequence for a reasonable Δt , large translations, rotations and perspective changes will not occur. As a result the tracking algorithm in Section 2.3 will obtain a one to one match between consecutive frames. Therefore the equation for ρ was modified to

$$\rho(\delta, r) = \frac{3(r^2 - \delta^2)}{4r^3}. \quad (12)$$

Finally the value of r as in [10], starts as a large number and decreases after each optimization of the objective function (8). The starting value for r was chosen as $3\Delta_{MAX}$ where Δ_{MAX} is the maximum possible displacement of an anchor point between frame T and $T+1$. This starting value of r is much smaller than the starting value recommended in [10] because very little deformation occurs between consecutive frames.

3. Mitosis Detection

The triangular mesh that is tracked from frame to frame essentially tracks the section of tissue inside each triangle from frame to frame. Given the location of all these small tissue segments, a study of the tissue's colour or intensity can be performed. Intensity decreases in tissue regions where mitosis is taking place. Therefore, by studying the intensity of each segment of tissue in the triangular mesh over multiple frames, all tissue segments that undergo an intensity change can be isolated. Then studying the magnitude of the intensity change, the size of the tissue segments that changed in intensity and the duration of the intensity change the locations of mitosis can be isolated.

The decrease in intensity of tissue segments between frames can be obtained as the difference in the average gray scale value inside corresponding triangles in the tracked triangular mesh. Given G_i^T , the average gray scale intensity for triangle i in frame T , the gray scale intensity decrease at frame T for triangle i , D_i^T , can be obtained as

$$D_i^T = G_i^T - \min(G_i^{T+1}, G_i^{T+2}, \dots, G_i^{T+Q}). \quad (13)$$

The value of Q is chosen such that it represents the duration of mitosis. All negative values of D_i^T are set to zero because only decreases in intensity are of interest. The difference values are then thresholded to obtain the locations of mitosis.

Several criteria can be used to threshold D_i^T : magnitude, spatial spread and temporal spread. First, mitosis tends to have a large decrease in intensity, whereas lighting changes will not produce such a large decrease in intensity. Secondly, if the triangles in the mesh are smaller than the cells, then areas of mitosis will have several adjacent triangles with large intensity change. Finally, since mitosis occurs over several frames, the areas of large intensity change will persist over multiple frames.

First a magnitude threshold defined in (14) is applied to D_i^T to obtain areas of large intensity changes.

$$\hat{D}_i^T = \begin{cases} 1 & D_i^T > G_i^T T_m + T_b \\ 0 & \text{Otherwise.} \end{cases} \quad (14)$$

Thresholding is based on the original average gray scale value of the triangle G_i^T , because sample data indicated that a bright cell will have a larger decrease in intensity during mitosis than a darker cell. The values of T_m and T_b are highly dependent on the quality of image. Currently they are selected by viewing a small sample of mitosis in a given image sequence.

Secondly the spatial spread of the detected regions in \hat{D}^T is thresholded. To perform thresholding on the spatial spread, a list of connected tissue segments with $\hat{D} = 1$ is obtained for each frame T as O^T . The size of each connected regions, hence forth referred to as objects, is determined as the number of triangles in each connected objects. A size threshold of T_L is applied to all objects in O^T such that all objects in O^T with less than T_L connected triangles are eliminated. T_L is chosen as the number of triangles that can fit within the width of the cell. In order to use this thresholding technique, the resolution of the triangular mesh must be fairly high. Since tracking a high resolution triangular mesh from frame to frame is computationally expensive, a low resolution mesh can be used for tracking then later interpolated to obtain a higher resolution.

Finally, the remaining objects in O^T are further pruned using the temporal spread of the objects. Given Q , the duration of mitosis and Y the time to the nucleus division (Figure 9) it can be estimated that there will be $Q - Y + 1$ frames where the large decrease in intensity can be detected during mitosis. As a result, any object in list O^T that are not present for $Q - Y + 1$ frames are deleted as false positive. An object in frame T is said to be present in frame $T + 1$ if any triangle from object O_i^T overlaps with a triangle from any object in frame $T + 1$.

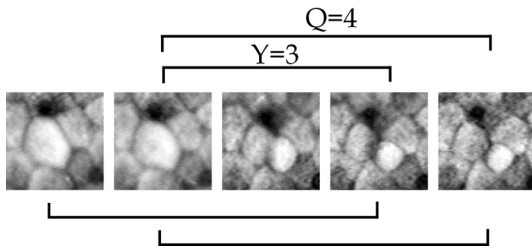


Figure 9. The time for mitosis and nucleus division is illustrated. The maximum decrease in intensity is seen two times ($Q - Y + 1 = 4 - 3 + 1 = 2$).

The remaining objects in O^T are the locations of mitoses. However, the total mitoses can not be obtained by

counting the objects in O^T because each object in O^T is detected over at least $Q - Y + 1$ frames. Therefore, the temporal location must be isolated before counting the number of mitoses. Currently the temporal location of a mitosis is set to the frame in which the object O_i^T first appears. The object is deleted in the consecutive frames before determining the mitosis count.

4. Testing & Results

A twenty frame test image sequence, taken over one hundred minutes, was used to evaluate the mitosis counting algorithm. Ninety-five mitosis locations were identified manually on the test image sequence. The performance of this algorithm is not compared with other algorithms as no existing algorithms for detecting mitosis in live tissues were found.

For the test images the parameters that were used are $T_m = 70/255$, $T_b = 5/255$, $T_L = 5$, $Q = 4$ and $Y = 2$. The parameters T_L , Q and Y are fixed to the size of the cells and the duration of mitosis. The values of T_m and T_b were estimated manually by studying the intensity change of mitoses. Though a full sensitivity study of T_m and T_b is not performed here, it was found that reasonable changes in these values did not significantly change the detection rate. Furthermore, these values can easily be estimated based on the division of a well illuminated cell and a poorly illuminated cell.

The classification results for the given parameters are presented as a confusion matrix in Figure 10. Some of the detected mitosis are illustrated in Figure 11. A frame from the image sequence is illustrated in Figure 12 with some intermediate data for tracking grid as well as detecting mitosis.

		Predicted	
		Positive	Negative
Actual	Positive	81	14
	Negative	21	N/A

Figure 10. Confusion matrix for mitosis detection.

From the confusion matrix, the true positive rate (TP) is found as 85% and the precision (P) is found as 79%. The accuracy can not be calculated from the confusion matrix without knowing the true negative classification quantity. Therefore the performance of the algorithm is found using the geometric mean [9] ($g - mean$) as 82%.

$$g - mean = \sqrt{TP * P} \quad (15)$$

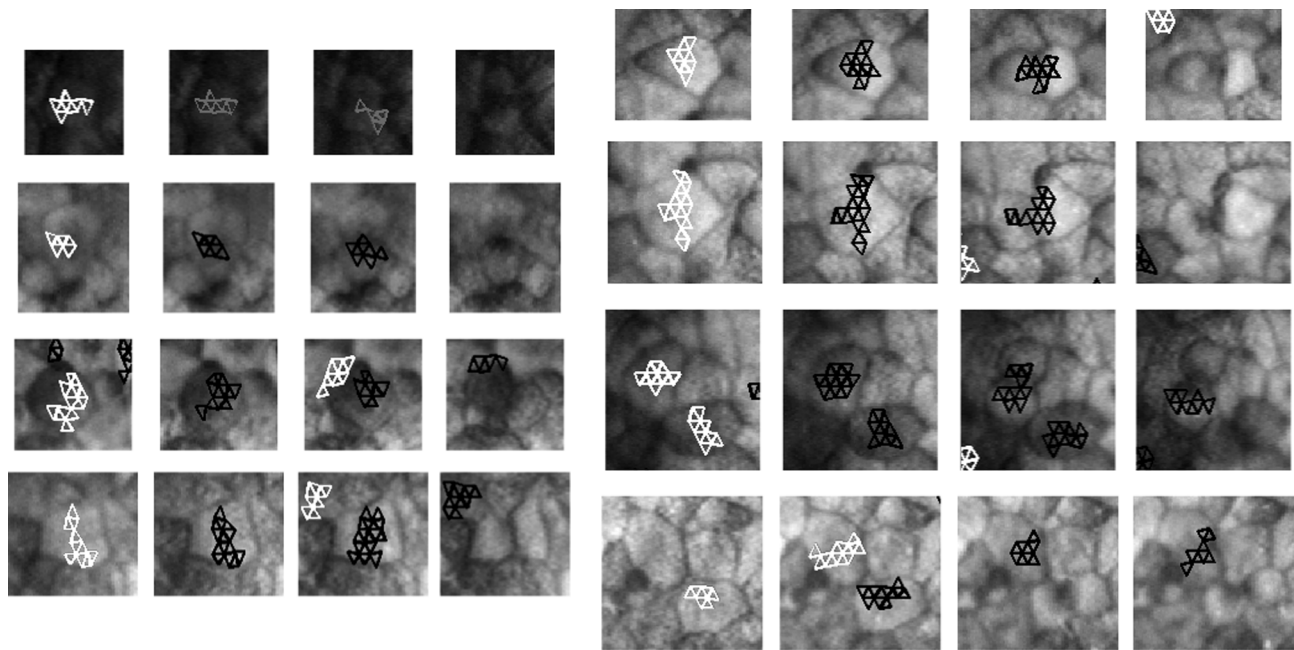


Figure 11. Consecutive frames with mitosis and the detection results. The triangular grids detected as mitosis are outlined in white or black. White is the start of a detected mitosis sequence and black is the subsequent detections of a detected mitosis.

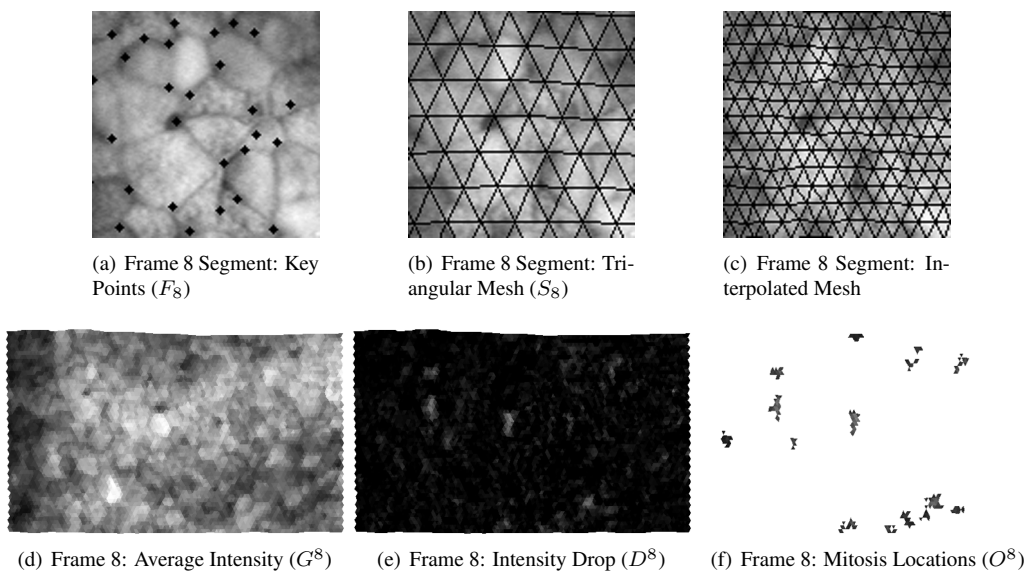


Figure 12. The intermediate and final results for frame 8 in the test image sequence.

There are two causes for the false negative rate. First, the intensity decrease during nucleus division was not high enough to be detected. This can be due to poor contrast and or focus changes during mitosis. Second, multiple mitoses in adjacent cells are detected as one. The intensity decrease of adjacent mitosis are joined together as one because the resolution of the triangular mesh is not high enough to detect the separation between the intensity drops.

False positives are caused by errors in tracking due to the density of the key points used in tracking the triangular mesh. When a cell divides, its neighbors shift positions slightly; the shift is confined to a local region. If there are no key points present in this local region, the motion will not affect the deformation of the triangular mesh. In some cases this results in the algorithm detecting the slight movement of a boundary between a light cell and a dark cell as an intensity drop caused by mitosis.

5. Future Work

Some of the false negatives and false positives are caused by illumination defects during imaging. These are difficult to compensate during mitosis detection, however, to correct for errors in detecting adjacent cell division and motion of cell boundaries between dark and light cells is possible.

The problem of adjacent mitosis detection is caused by a lack of triangular mesh resolution. Therefore, for all mitosis locations detected by triangular mesh difference, a pixel-by-pixel difference in intensity can be calculated within the triangular mesh. This will not be as computationally expensive as performing pixel-by-pixel intensity difference for the entire image and can potentially increase the resolution sufficiently to separate the multiple mitosis.

After mitosis, the region where the cell divided will have a boundary (*line*) between the two new child cells. If there is an intensity drop caused by the motion of a cell boundary, the location of the intensity drop will not have a new boundary. By detecting the presence of a new boundary after mitosis, the false positives caused by the motion of cell boundaries can be reduced.

6. Conclusions

An algorithm for identifying mitosis in time lapse images of live embryonic tissue is presented. Unlike previously published research, which classify mitosis as the darkest region in the image, the presented algorithm uniquely uses temporal information to detect mitosis. By using the temporal intensity change of cells during mitosis, the presented method can detect mitosis automatically even when the mitosis regions are not the darkest regions in the image.

The algorithm tracks the overall motion and deformation of the embryonic tissue with a triangular mesh before detecting mitosis by looking for intensity drops associated with division. The algorithm achieved a performance of 82%. The algorithm presented here is expected to significantly enhance the evaluation of the role of mitosis in early embryo development.

References

- [1] G. W. Brodland and J. H. Veldhuis. Computer simulations of mitosis and interdependencies between mitosis, cell shape and epithelium reshaping. *Journal of Biomechanics*, 35:673–681, 2002.
- [2] D. A. Clausi and G. W. Brodland. Mechanical evaluation of theories of neurulation using computer simulation. *Development*, 118:1013–1023, 1993.
- [3] E. R. Dougherty and R. A. Lotufo. Hands-on morphological image processing. page 290, 2003.
- [4] D. J. Fleet, A. D. Jepson, and M. R. M. Jenkin. Phase-based disparity measurement. *Computer Vision, Graphics, and Image Processing. Image Understanding*, 53(2):198–210, 1991.
- [5] M. S. Grewal and A. P. Andrew. *Kalman Filtering: Theory and Practice*. Prentice Hall, 1993.
- [6] P. Iles. Average cell orientation, eccentricity and size from tissue images. Master's thesis, University of Waterloo, Waterloo, Ontario, Canada.
- [7] E. J. Kaman, A. W. M. Smeulders, P. W. Verbeek, I. T. Young, and J. P. A. Baak. Image processing for mitoses in sections of breast cancer: A feasibility study. *Cytometry*, 5(3):244–249, 1984.
- [8] T. K. t. Kate, J. A. M. Belien, A. W. M. Smeulders, and J. P. A. Baak. Method for counting mitoses by image processing in feulgen stained breast cancer sections. *Cytometry*, 14(3):241–250, 1993.
- [9] M. Kubat, R. C. Holte, and S. Matwin. Machine learning for the detection of oil spills in satellite radar images. *Machine Learning*, 30(2-3):195–215, 1998.
- [10] J. Pilet, V. Lepetit, and P. Fua. Real-time non-rigid surface detection. In *IEEE Computer Society Conference on Computer Vision and Pattern Recognition (CVPR)*, volume 1, pages 822–828, 2005.
- [11] H. H. Refai, L. Li, T. K. Teague, and R. Naukam. Automatic count of hepatocytes in microscopic images. In *International Conference on Image Processing*, pages II: 1101–1104, Barcelona, Spain, 2003.
- [12] A. Singh. *Optic Flow Computation: A Unified Perspective*. IEEE Computer Society Press, 1992.
- [13] A. Talukder and C. D. P. Multiscale gabor wavelet fusion for edge detection in microscopy images. *SPIE*, 3391(1):336–347, 1998.
- [14] J. H. Veldhuis and G. W. Brodland. A deformable block-matching algorithm for tracking epithelial cells. *Image and Vision Computing*, 17:905–911, 1999.
- [15] L. M. Vincent and M. B. R. Morphological image processing and network analysis of cornea endothelial cell images. *SPIE*, 1769:212–226, 1992.